The Cryosphere Discuss., 9, 1461–1502, 2015
www.the-cryosphere-discuss.net/9/1461/2015/
doi:10.5194/tcd-9-1461-2015

The Cryosphere
Discussions
Open Access

# Assimilation of Antarctic velocity observations provides evidence for uncharted pinning points

**J. J. Fürst[1], G. Durand[1], F. Gillet-Chaulet[1], N. Merino[1], L. Tavard[1], J. Mouginot[2], N. Gourmelen[3], and O. Gagliardini[1,4]**

[1]UJF — Grenoble 1/CNRS, Laboratoire de Glaciologie et Géophysique de l'Environnement (LGGE) UMR 5183, Grenoble, France
[2]University of California, Department of Earth System Science, Irvine, USA
[3]The University of Edinburgh, School of GeoSciences, Edinburgh, UK
[4]Institut Universitaire de France, Paris, France

Received: 16 February 2015 – Accepted: 17 February 2015 – Published: 5 March 2015

Correspondence to: J. J. Fürst (johannes.fuerst@lgge.obs.ujf-grenoble.fr)

Published by Copernicus Publications on behalf of the European Geosciences Union.

## Abstract

In ice flow modelling, the use of control methods to assimilate the dynamic and geometric state of an ice body has become common practice. These methods have primarily focussed on inverting for one of the two least known properties in glaciology, namely the basal friction coefficient or the ice viscosity parameter. Here, we present an approach to infer both properties simultaneously for the whole of the Antarctic ice sheet. During the assimilation, the root-mean-square deviation between modelled and observed surface velocities is reduced to $12.3\,\mathrm{m\,a^{-1}}$, with a value of $16.4\,\mathrm{m\,a^{-1}}$ for the ice shelves. An exception in terms of the velocity mismatch is the Thwaites Glacier ice shelf, where the RMS value attains almost $80\,\mathrm{m\,a^{-1}}$. The reason is that the underlying BEDMAP2 geometry ignores the presence of an ice rise, that exerts major control on the dynamics of the eastern part of the ice shelf. On these grounds, we suggest an approach to account for pinning points not included in BEDMAP2 by locally allowing an optimisation of basal friction during the inversion. In this way, the velocity mismatch on the Thwaites ice shelf is more than halved. A characteristic velocity mismatch pattern emerges for unaccounted pinning points close to the marine shelf front. This pattern is exploited to manually identify 7 uncharted features around Antarctica that exert significant resistance to the shelf flow. Potential pinning points are detected on Fimbul, West, Shakelton, Nickerson and Venable ice shelves. As pinning points can provide substantial resistance to shelf flow, with considerable consequences if they became ungrounded in the future, the model community is in need of detailed bathymetry there. Our data assimilation points to some of these dynamically important features, not present in BEDMAP2, and implicitly quantifies their relevance.

## 1 Introduction

More than 60 % of the grounded parts of the Antarctic ice sheet extends into a distinct floating ice shelf (Fretwell et al., 2013). A minority of these shelves can be considered to be mostly unconfined, which implies that their influence on the upstream ice flow is limited (e.g. Schoof, 2007). The vast majority is however confined and exerts control on the upstream ice flow and by extension on the ice discharge from the grounded ice sheet. Ice discharge is the flux over the grounding line (e.g. Shepherd et al., 2012; Depoorter et al., 2013), which itself is the delineation of where the ice body starts to float on its way to the ice-sheet margin. Changes in ice discharge rates quantify the dynamic contribution of the ice sheet to sea-level (Rignot et al., 2008), because it is there where the ice overburden is no longer supported by an underlying bed. As most shelves are well confined, a reduction or even a loss in the resistance provided by these confinements is expected to trigger an abrupt increase in ice discharge and thus in rates of sea-level contribution (Favier et al., 2012).

An ice shelf confinement can simply be an embayment formed either by promontories or by ridges with grounded ice protruding from the ice sheet. In such a setup, the shelf experiences high lateral resistance (Thomas, 1979). This resistance is directly identifiable from pronounced cross-flow gradients in the observed surface velocities. Other confinements are embedded within floating ice shelves and are thus disconnected from the hinterland. For these pinning points, the ice shelf locally runs aground and the bed contact provides friction at the basal interface. Pinning points often give rise to longitudinal resistance, i.e. a pressure acting on a plane perpendicular to the ice flow. Any form of resistance imposed on the membrane-like flow regime of an ice shelf is often referred to as buttressing (Hindmarsh, 2006; Schoof, 2007). In general, there are three distinct classes of pinning points (e.g. Armstrong et al., 1977; Thomas, 1979): ice rises, ice rumples and ephemeral ice rumples. Ice rises show a rather strong basal contact and they are characterised by a locally defined flow regime which is normally well expressed in the surface topography. For ice rumples, the contact is weaker and thus the flow regime is primarily determined non-locally by the dynamic state of the surrounding ice shelf. Ice rumples are called ephemeral if there is evidence that the weak bed contact is not permanent. Ocean tides, for instance, give rise to such intermittent contact. In any case, pinning points do not necessarily require a large horizontal extent to significantly alter the large-scale shelf flow.

When assimilating observations on the geometric and dynamic state of an ice sheet with a flow model, special attention has to be payed to potential pinning points as their influence on the shelf dynamics can reach far. In glaciological modelling, data assimilation often takes the observed geometry as granted and tries to optimise unknown model parameters to minimise the mismatch to other observations (e.g. MacAyeal, 1993). For this purpose, inverse methods or control methods have been suggested that aim at minimising differences between observed and modelled surface velocities under a given geometry (MacAyeal, 1993). Based on Antarctic-wide compilations of ice geometry and surface velocities (Rignot et al., 2011b; Fretwell et al., 2013), Morlighem et al. (2013) and Arthern et al. (2015) have shown that inverse methods are feasible at continental scale. Both studies use a state-of-the-art ice flow model to infer the largely unknown basal friction beneath the grounded part of the Antarctic ice sheet. They find that low friction is widespread and can indeed reach far inland along tributary glaciers and ice streams. Here, we want to pursue a similar approach to assimilate velocity observations but we aim at a better quantification and understanding of remaining velocity differences. If the assimilation showed a non-local mismatch on an ice shelf, this would be a first indicator that a pinning point might be ignored in the geometry data set.

In principle, remaining velocity differences can arise from three main sources during the data assimilation. They can originate from the optimisation procedure, from the ice flow model or from the actual measurements. In the first case, the optimisation might suffer from a bad choice of the cost function or an excessive regularisation term. Moreover convergence has to be guaranteed. Second discrepancies can arise from the underlying flow model. This can imply that the model physics is not appropriate to describe the observed flow behaviour. In this case, the model might rely on approximations not suitable for a particular flow regime or it ignores essential processes. Another point is that the model resolution has to be chosen compatible with the observations. Finally, remaining discrepancies might be linked to the observational input. If so, measurements might come at large uncertainties which intrinsically impedes a good reproduction. In order to capture the spatial variability of observed surface velocities, the resolution of the geometry input has to be sufficiently fine. In large data compilations, any inconsistencies between different data sources or simple local incompleteness might also give reason to biases. In regions where fast changes are observed, acquisition dates of ice flow and geometry should be as contemporaneous as possible.

In this study, we apply control methods on the recent data sets for Antarctic-wide ice geometry and surface velocities (Sect. 2). The aim is to assess the origin of remaining differences between the observed and modelled velocities (Sect. 3). It is found that mismatches are most expressed on the ice shelves, in areas where pinning points are missing in the geometry data (Sect. 3.4). We suggest an approach to account for these pinning points in the inversion (Sect. 3.5), and use a characteristic mismatch pattern to identify, to this day, uncharted pinning points (Sect. 3.6).

## 2 Model description

### 2.1 Ice flow model

Elmer/Ice is an open-source 3-D thermo-mechanically coupled ice flow model (Gagliardini and Zwinger, 2008; Gillet-Chaulet et al., 2012; Gagliardini et al., 2013) and the glaciological extension of the Elmer finite element software developed at the CSC-IT Center for Science in Finland (http://www.csc.fi/elmer/). It is an efficient, state-of-the-art tool to solve the full complexity of the underlying force balance equations.

As we put the focus on the floating parts of the ice sheet, a model variant is applied that solves the shallow shelf approximation (SSA; e.g. MacAyeal, 1989). In this approximation, gravitational driving is balanced by friction at the base and horizontal alignment of the local flow into the dynamic state of the surrounding ice. This alignment is communicated by gradients in membrane stresses (Hindmarsh, 2006). On the floating shelves, basal friction is negligible and the membrane stress effect exclusively depends on the effective viscosity $\eta$ of the material. The effective viscosity comprises the non-linearity in the constitutive equation, which links the deviatoric stress field $\boldsymbol{\tau}$ to ice deformation.

$$\eta = \frac{1}{2} \cdot B \cdot \varepsilon_e^{(1-n)/n} \tag{1}$$

Here, $\varepsilon_e = \sqrt{\varepsilon_{ij} \cdot \varepsilon_{ij}/2}$ is the second invariant of the strain rate tensor $\boldsymbol{\varepsilon}$. We assume isotropic material properties and a flow exponent of $n = 3$. For shelf dynamics, $B$ is sometimes referred to as ice rigidity (e.g. Borstad et al., 2013; Larour et al., 2014). Yet, terms as rigidity and stiffness are strictly associated with elastic deformation. As $B$ determines the readiness of the viscous material to deform under a given stress, $B$ is here referred to as the viscosity parameter (Van Der Veen, 1999). To facilitate readability, we will likewise refer to it as the ice viscosity, though this is only the case for linearity in the constitutive equation, i.e. a Newtonian fluid.

At the ice–bedrock interface, a Coulomb-like friction law is applied (Paterson, 1994):

$$\boldsymbol{\tau}_{\mathrm{b}} = \beta^2 \cdot \boldsymbol{v}_{\mathrm{b}}, \tag{2}$$

where $\boldsymbol{\tau}_{\mathrm{b}}$ and $\boldsymbol{v}_{\mathrm{b}}$ are vectors tangential to the glacier base respectively for basal shear stress and ice velocity. $\beta^2$ denotes the positively defined basal friction coefficient.

## 2.2 Mesh

The analysis presented here will focus on ice shelves, ice streams and fast outlet glaciers. Anisotropic mesh adaptation allows us to refine the grid in these regions (Morlighem et al., 2010; Gillet-Chaulet et al., 2012). First we distinguish between floating and grounded parts of the ice sheet, for which the target resolutions are respectively 1.4 and 50 km. For any location away from the grounding line, the final grid shows a nominal resolution close to these values. The decrease in resolution takes actually place upstream of the grounding line and spans a band of roughly 100 km. In addition to this, the grid is refined in areas where flow magnitudes exceed 100 m a$^{-1}$. There, the refinement follows the Hessian matrix of the observed velocities (Morlighem et al., 2010; Gillet-Chaulet et al., 2012). In this way, maximum resolution is ensured for both the floating fringes of Antarctica and the main tributaries.

### 2.3 Control method

On the basis of the SSA equations, we simultaneously infer basal friction $\beta^2$ and ice viscosity $B$ using control methods building on the approach described in Gillet-Chaulet et al. (2012) and Gagliardini et al. (2013). In contrast to their methodology, we conduct a dual inversion as in Arthern et al. (2015). Additionally, we adjust the cost function and start from a physically based initial guess for the two inversion variables. Convergence of the optimisation is assumed to be reached after 750 iterations.

The total cost function $J$ comprises the velocity mismatch and two regularisation terms.

$$J = J_0 + \lambda_{\beta^2} \cdot J_{\beta^2}^{\mathrm{reg}} + \lambda_B \cdot J_B^{\mathrm{reg}} \tag{3}$$

The mismatch between modelled and observed velocities is comprised in the first cost term $J_0$. Here, we use the original form suggested in MacAyeal (1993), that accounts for differences in both horizontal velocity components. During the inversion, we actually optimise multiplier fields $m_B$ of the form $B = m_B^2 \cdot B_{\mathrm{ini}}$ (also see Gillet-Chaulet et al., 2012). The applied regularisation in turn penalises first spatial derivatives in the respective muliplier fields $m_{\beta^2}$ and $m_B$. The two additional terms $J_{\beta^2}^{\mathrm{reg}}$, $J_B^{\mathrm{reg}}$ are added to the total cost $J$. They improve the conditioning of the underlying problem by suppressing over-fitting of the velocity observations.

Since there is an interdependence when inverting for two variables simultaneously, the inferred fields are dependent on the initial guess (Arthern and Gudmundsson, 2010). To guarantee that the inferred variables remain in a physical range, the initial fields have to be selected with care. The initial guess for $\beta^2$ is found by assuming that basal drag equals the local driving stress. From another inversion of basal friction on Antarctica (Morlighem et al., 2013), we know that over most of the ice sheet interior these two are nearly equal. There, the initialisation of $\beta^2$ is expected to strongly facilitate the convergence of our optimisation. In regions, where the ice flow becomes channelised and the large-scale character of ice-sheet dynamics is violated, this intialisation is less appropriate.

The initial field for the ice viscosity parameter $B$ is inferred from an ice temperature reconstruction (Van Liefferinge and Pattyn, 2013), using a standard Arrhenius relation (Paterson, 1994). To test whether the inversion is sensitive to the intial temperature-based (TB) guess, we employ two options to replace these values on the ice shelves following Borstad et al. (2013). Avoiding their formal usage of flow-line theory, $B$ is determined by equating the force exerted in flow direction by ice deformation (the latter known from strain rates) with the vertically integrated hydrostatic back pressure. This new $B$ field is referred to as the hydrostatically balanced (HB) viscosity. In its original form, Borstad et al. (2013) exclusively used this HB viscosity where values are lower than the TB field. As this correction is motivated from identifying the state of ice damage on floating shelves, we refer to this initial $B$ field as the damage-corrected (DC) viscosity.

## 2.4 Observational input

### 2.4.1 Ice sheet geometry

The ice sheet geometry is based on the recent BEDMAP2 data compilation, presented at 1 km resolution (Fretwell et al., 2013). The BEDMAP2 thickness map is inferred from roughly 25 million measurements, with about 2.5 % of cross-over information. Analysis of all cross-overs indicates that 50 % of the measurement differences fall in a 5 m window around the median at −1 m. As data were collected over several decades, this agreement seems to justify the assumption that changes in the ice sheet geometry through time are comparably small with respect to the measurement uncertainty. However, the standard deviation in the cross-over differences is stated with 50 m, suggesting that a non-negligible amount of data either comes at higher measurement uncertainty, is biased by the mission-specific methodology, or simply suffers from geometric changes over time. In the Amundsen sea embayment, recent surface elevation changes are most expressed (Pritchard et al., 2009, 2012). In the frontal area of Pine Island Glacier (PIG), a 2011 survey had to be excluded from BEDMAP2, as thinning reached 40 m with respect to more extensive earlier surveys conducted in 2004/05 (Vaughan et al., 2006; Holt et al., 2006).

The BEDMAP2 surface elevation, bedrock elevation, ice thickness and a given mask, for whether ice is grounded or afloat, are interpolated onto the model grid. For the Antarctic ice shelves, flotation needs to be assured in the model. The reason is that otherwise a bias is introduced on the hydrostatic back pressure propagating into the inversion. In any prognostic application, the geometry would immediately be put afloat in the flow model. The most direct option is to locally adjust the density of the ice column according to flotation (case abbreviated with $\mathbb{D}$). This option has the advantage that no changes have to be applied to the BEDMAP2 geometry product. If one accepts prior changes in the geometry, BEDMAP2 offers three variables on the ice geometry, i.e. the upper and lower ice shelf surfaces and the ice thickness. After prescribing one of them, the other two will follow from the standard model densities for sea water and ice, respectively at 1028 and 917 $\mathrm{kg\,m^{-3}}$. The three options are thus the prescription of either the thickness ($\mathbb{T}$), the upper surface ($\mathbb{U}$) or the lower surface ($\mathbb{L}$) from observations. All these options were implemented under the condition that the ice base did not exceed the bedrock topography. Independent of these geometric changes, the original BEDMAP2 mask is used to delineate the area where no basal friction is applied.

Following option $\mathbb{D}$, a spatially variable density field with a shelf-average of 865 $\mathrm{kg\,m^{-3}}$ is obtained. The derived density field shows however areas in which values exceed the density of most compact marine ice 940 $\mathrm{kg\,m^{-3}}$ (e.g Craven et al., 2009) or fall below typical values for dense firn of 700 kg m$^{-3}$. Either way, these values are beyond the physical range as they are representative for the entire ice column. Therefore, details in this generic density field should not be interpreted in terms of snow/ice transformation. As the standard model density lies higher, adjustment of the geometry to a prescribed thickness field ($\mathbb{T}$), results in a general lowering of the surface elevation, with an average of 15 m. If the upper ($\mathbb{U}$) or lower surface ($\mathbb{L}$) is prescribed, the shelf thickness is either increased or decreased by comparable values.

### 2.4.2 Surface velocities

Information on the dynamic state of the entire Antarctic ice sheet was recently brought together and presented in a single database by Rignot et al. (2011b). Surface velocity magnitudes were inferred from synthetic aperture radar (SAR) imagery acquired between 1996 and 2009 with five different satellite-mounted sensors. The coverage of this velocity mosaic is almost complete and errors in the inferred flow field fall below 10 m a$^{-1}$ over most of Antarctica. We do not use the later released high resolution data, but base ourselves on the earlier product with a 900 m sample spacing as the inversion is limited by the 1 km BEDMAP2 geometry. The velocity components are not interpolated on the model grid but directly used, because, during the optimisation, differences with the simulated flow field are calculated at the data locations in the velocity mosaic.

### 2.4.3 Additional grounding line information

Independent information on grounding line migration between 1994 and 2009, derived from differential satellite SAR interferometry (DInSAR), is available as cross-validation for BEDMAP2 (InSAR) (Rignot et al., 2011a). This data set allows the localisation of additional pinning points not included in the BEDMAP2. Though already identified in 2001 (Rignot, 2001; Rignot et al., 2014), a large ice rise on the eastern ice shelf of Thwaites Glacier (TWG) does not appear in BEDMAP2 due to a lack of bathymetry data in this region. The friction this ice rise exerts at the shelf base is well imprinted in the surface velocity field, as flow speeds there are extremely low. A delineation of this ice rise, as in Rignot et al. (2014), was available. Not as influential, but also missing in BEDMAP2 and Rignot et al. (2011a), Bawden ice rise (BIR) is situated on the north-eastern marine front of Larsen C (LC) ice shelf (Borstad et al., 2013). We manually delineated the BIR using ALOS/PALSAR imagery.

## 3 Results

Using exclusively the BEDMAP2 geometry, we first address the dependence of the dual inversion on the initialisation of the optimised parameters and their regularisation. Thereafter, different options to impose flotation on the model geometry are assessed in terms of the consequences for the inferred $B$ field (Sect. 3.2). For this comparison, the well-studied Larsen C (LC) shelf is chosen. Selecting the $\mathbb{T}$-geometry, we then pursue a more global assessment of the velocity mismatch after the inversion (Sect. 3.3). For a few exclusive shelves, it is possible to qualitatively compare the performance of the inversion in terms of ice viscosity and velocity mismatch. Complementary information on grounding line positions is used to locate pinning points missing in BEDMAP2, which allows to discern a characteristic pattern in the velocity mismatch (Sect. 3.4). We then assimilate these complementary information in our inversion by allowing a local optimisation of the friction coefficient at these positions (Sect. 3.5). In a final step, we identify other potential pinning points not included in the data sets at hand (Sect. 3.6).

### 3.1 Initialisation and regularisation

During the iterative optimisation of the cost function, its initial value is decreased by more than 3 orders of magnitude. This primarily reduces the mismatch between modelled and observed velocities (Fig. 1). The simultaneous inversion of two parameters seems sufficiently well conditioned, by the regularisation and the fact that the inversion is limited to the viscosity parameter $B$ on the ice shelves. The multiplier for the friction field $m_{\beta^2}$ is characterised by values close to unity for most of the ice sheet interior. Along regions of fast ice flow, the inversion finds however very low values, as confirmed by an earlier inversion on continental scale (Morlighem et al., 2013; Arthern et al., 2015). The multiplier field $m_B$ for the ice viscosity generally falls into the range of 0.1 and 10. Altogether this suggests that both initial fields are well chosen in view of this dual inversion.

As our later assessment will focus on the performance of the inversion on the ice shelves, the sensitivity of the inferred viscosity is assessed under three initial fields, that differ only on the floating parts (Sect. 3.1). The final pattern and magnitude of the viscosity $B$ compare well, independent on which of the initial fields is chosen. They also result in similar root-mean-square (RMS) deviation values for single shelves and the entire ice sheet (Table 1). Locally however, where the DC and the HB option prescribe a very low viscosity parameter, the inversion is not able to revert this initial bias. These similarities assure us that the viscosity inversion on the shelf is rather well-conditioned.

In order to retrieve an appropriate parameter combination for $\lambda_{\beta^2}$ and $\lambda_B$, we rely on the L-curve method (e.g. Hansen, 1992; Jay-Allemand et al., 2011; Morlighem et al., 2013, and references therein). The L-curve gives a means to find a trade-off between fitting a target quantity while keeping a certain smoothness in the optimised variable. In our case, we define a L-surface quantifying the mismatch between observed and modelled velocities $J_0$ as a function of the two regularisation terms $J_{\beta^2}^{\text{reg}}$ and $J_B^{\text{reg}}$ (Fig. 2). Each position on this plot is associated with one parameter combination and the sampling is equally spaced in a logarithmic sense. The L-surface allows the identification of an area in parameter space avoiding two extremes: either overfitting of the velocity observations or excessive regularisation that dominantes the cost function $J$. The exact parameter choice depends on the later purpose of the inverted fields. As our interest is in the velocity mismatch, which is correlated to $J_0$, we choose the combination for which $J_0$ is minimised, and thus $\lambda_{\beta^2} = 10^5$ and $\lambda_B = 10^3$.

## 3.2 Geometry at flotation

In general, any option for imposing flotation on the shelf geometry in the model results in lower ice viscosity from the inversion as compared to the unadjusted case (Fig. 3a and b). The reasoning however depends on the details of how flotation is imposed. For case $\mathbb{D}$, shelf densities are generally lower, resulting in less gravitational forcing, which is compensated by a viscosity decrease in order to balance the same hydrostatic back pressure. In case $\mathbb{T}$, the ice shelf volume beneath sea-level is higher than in the original BEDMAP2 geometry, resulting in an increased hydrostatic back pressure, compensated by lowering $B$. When the bottom shelf surface is prescribed $\mathbb{L}$, the back pressure is the same as for the original BEDMAP2 data set. However, the shelf thickness and with it the driving stress are reduced, compensated in our inversion by a decrease in the viscosity parameter. The last case $\mathbb{U}$ is a combination of increasing both the driving stress and the back pressure simultaneously by thickening the shelf ice. As this results in lowest $B$ values, the influence of the increased water back pressure seems dominant. In cases $\mathbb{T}$ and $\mathbb{L}$, the pursued adaptations of the shelf geometry also result in steeper surface gradients. Their influence seems however negligible compared to the simultaneous effect from increasing back pressure by surface lowering in $\mathbb{T}$ or decreasing driving stress by thinning in $\mathbb{L}$.

The RMS deviation between observed and modelled surface velocities will serve to assess which of the options for putting the shelves afloat is favourable (Table 1). The best fit is accomplished when the shelf thickness $\mathbb{T}$ is kept while adjusting the upper and lower surfaces according to the model ice density. If we break down the RMS deviation into the floating and grounded parts of the ice sheet, option $\mathbb{T}$ shows best performance. Even for many individual ice shelves, the mismatch is minimal in this case. On LC, there are some locally confined, cross-flow features upstream of Griggs ice rise, where velocity gradients in flow-direction are very high. These features were associated with damaged ice and thus low viscosity (Borstad et al., 2013). Using the $\mathbb{T}$-geometry, the inversion is facilitated and shows most pronounced reduction of $B$ for these features (Fig. 3b). Observed and modelled velocities are also in better agreement in this region (Fig. 3e).

In principle, the $\mathbb{D}$-, $\mathbb{U}$- and $\mathbb{T}$-options give very similar results even though the latter shows the overall best performance. Here, we kept standard values for ice and ocean density, limiting the validity of the comparison. However, the $\mathbb{T}$-geometry adjustment has two additional advantages. First, it preserves the ice volume from the data compilation. Second, as compared to the $\mathbb{D}$-option, forward modelling is not faced with how to advect a generic density field. In the following, our inversion is based on the $\mathbb{T}$-geometry.

## 3.3 General performance

In general, the inferred velocity field is in good agreement with observations (Fig. 1). The RMS differences between observed and modelled velocities reaches 12.4 $\mathrm{m\,a^{-1}}$ for the whole of the Antarctic ice sheet (Table 1). Remaining discrepancies are either spatially confined or, if widespread, small in magnitude. A similar inversion for the whole of Antarctica shows a saturation of the bulk RMS deviation at $\sim 40\,\mathrm{m\,a^{-1}}$ (Arthern et al., 2015). As they constrain the inversion not only by observations on surface velocities, but also on accumulation rates and surface elevation changes, it is only natural that we obtain a better match in terms of velocities. Here, we did not follow their suggestions, as we do not want to intialise the flow model for transient similations. The aim is rather to identify locations where the model is not able to reproduce observed ice flow.

The velocity mismatch on the grounded part of the ice sheet is smaller than on the floating parts, with RMS values of respectively 11.7 and 16.7 $\mathrm{m\,a^{-1}}$ (Table 1). In large parts of the ice sheet interior, differences become very small (Fig. 1), justifying the choice for a coarse grid. However, the coarse resolution becomes insufficient for some channelised flow features. The velocity observation come at 900 m sample spacing and they are directly used in the optimisation. Therefore, a general mismatch pattern emerges for such channelised flow: underestimation of observed velocities in the centre of these channels and overestimation of the lateral flow speeds. It is also apparent that where these channelised features approach the grounding line, the mismatch decreases and often vanishes as a direct consequence of the increasing resolution.

The Filchner-Ronne ice shelf (FR) is the second largest and distinct floating unit of Antarctica. In an attempt to determine the complex rheology of the larger Ronne section of this shelf, Larour et al. (2005) used a similar inversion technique to determine $B$. Having put the shelf geometry afloat, they find values that vary between 0.3 and $0.9\,\mathrm{MPa\,a}^{1/3}$ confirming the range found here (Fig. 4). We also find soft ice in the elongated shear bands at both lateral shelf margins. With the increasing knowledge on ice velocities, our inversion is able to provide a viscosity map much richer in small-scale features. Turning towards difference between observed and modelled velocities, the early study states a bulk mismatch of $50\,\mathrm{m\,a}^{-1}$. Here, we find a value of $15\,\mathrm{m\,a}^{-1}$ for the entire FR ice shelf. Since the underlying velocity observations rely on different sensor products, these two values are not directly comparable. In most areas however, associated errors on these observations fall below $10\,\mathrm{m\,a}^{-1}$ (Joughin, 2002; Rignot et al., 2011b). Consequently, the threefold decrease in the bulk mismatch is rather a result from differences in the applied control methods.

After the disintegration of Larsen B in 2002 (MacAyeal et al., 2003), many studies were directed towards assessing the dynamic conditions preceding this event or monitoring the consequences for the tributary glaciers (Scambos et al., 2004; Vieli et al., 2006; Khazendar et al., 2007; Vieli et al., 2007; Rott et al., 2011; Berthier et al., 2012). In addition, the LC ice shelf received some attention, being the next ice shelf in line just south of Larsen B (Jansen et al., 2010; Borstad et al., 2013; Kulessa et al., 2014). Prescribing a constant viscosity $B$ of $0.42\,\mathrm{MPa\,a}^{1/3}$ for the entire shelf, Jansen et al. (2010) succeed in reproducing the general pattern and magnitude of the velocity field. The match is convincing in the central part of the ice sheet, and the general tendency to underestimate observed velocities becomes most apparent in the southern parts of the shelf. As the viscosity parameter is spatially optimised, our inversion is free of such a regional bias (Fig. 3e). In fact, regions where ice velocities are either over- or underestimated cover almost exactly the same area. In addition, the bulk RMS deviation is

$13\,\mathrm{m\,a^{-1}}$ and lies thus lower than the average mismatch for all Antarctic shelves (Table 1). In a more recent study, the LC viscosity parameter was inferred with the aim to identify regions of damaged ice (Borstad et al., 2013). In general, comparable $B$ fields were found (C. P. Borstad, personal communication, 2014), though we cannot confirm the elongated areas of soft ice downstream of the main promontories (Fig. 3b).

The Brunt/Stancomb-Wills (BSW) ice shelf is situated on the Caird Coast in Oates Land and it has been subject to several studies as it shows a very complex system of ice rifts, faults and pronounced shear margins (e.g. Humbert et al., 2009; Khazendar et al., 2009; Larour et al., 2014). Assuming a single $B$ value for the entire shelf, Humbert et al. (2009) find that observed velocities are best reproduced using $B = 0.35\,\mathrm{MPa\,a^{1/3}}$. A shelf average of our viscosity map gives a slightly more elevated value of $0.40\,\mathrm{MPa\,a^{1/3}}$. This earlier study also assessed a lowering $B$ along rifts and shear margins. They show that a local softening along these features can increase downstream flow magnitudes significantly. Our approach naturally finds low viscosity along these features and more viscous ice elsewhere (Fig. 5), which explains the higher shelf average. For the southwestern fringe of the BSW ice shelf, namely the Brunt ice shelf, Humbert et al. (2009) find a bulk velocity misfit with observations of $\sim 60\,\mathrm{m\,a^{-1}}$. Recently, a more physical approach was undertaken to capture the impact of rifts and faults in a flow model (Larour et al., 2014). In this approach, no lowering of the ice viscosity parameter is required for these features. Their inversion attains a shelf-wide velocity mismatch of $50\,\mathrm{m\,a^{-1}}$ which is almost three times higher than the value found here (Table 1). In contrast to Humbert et al. (2009) and our results, Larour et al. (2014) find more viscous ice ($\sim 0.54\,\mathrm{MPa\,a^{1/3}}$) in both cases, with and without accounting for ice rift/fault physics.

Highest surface velocities beyond $3000\,\mathrm{m\,a^{-1}}$ are observed in the Amundsen Sea Sector (ASS) and more specific for Pine Island Glacier (PIG) and Thwaites Glacier (TWG). For the central part of the PIG ice shelf, differences between simulated and observed flow velocities are efficiently reduced (Fig. 6). Yet for the lateral shear margins, the mismatch exceeds 100 $\mathrm{m\,a^{-1}}$, with different sign on each side of the fast-flow unit of the ice shelf. As this alternating pattern is identified for several other fast outlet glacier all around Antarctica, it is symptomatic and might indicate resolution issues, a regional under-convergence or a systematic minimum in the cost function for such setups. Another reason might be that the flow model is limited by the assumption of a continuous material, which might be violated in these areas of high crevassing. Turning to the ice viscosity, the inferred map shows two bands of very low values along these shear margins (not shown). Using a similar approach, Joughin et al. (2010) inverted comparable zones of weak ice in these areas. On the shelf of TWG, a strong across-flow gradient in surface velocities is observed. Despite this gradient, our inversion finds no pronounced band of low viscosity. However, we infer untypically viscous ice for the central eastern part of the ice shelf, where values readily exceed 2.00 $\mathrm{MPa\,a^{1/3}}$. In addition, the $\sim 80\,\mathrm{m\,a^{-1}}$ shelf-wide RMS velocity deviation is exceptionally elevated, with highest differences in this eastern region. At the source of these extreme values is a unconsidered contact between the bottom ice surface and the bathymetry.

### 3.4 Mismatch pattern near unaccounted pinning points

The presented inversion is capable of adequately reproducing observed ice velocities for the majority of ice sheet. Pronounced remaining differences are spatially very confined, while some features we attributed to a lack in model physics or coarse model resolution (Sect. 3.3). We conclude that the optimisation procedure is sufficiently converged, as RMS differences attain a low level. On the shelves and away from the grounding line, the SSA is an appropriate description for ice dynamics. There, remaining differences between modelled and observed velocities likely arise from observational inconsistencies. In this section, we will therefore characterise a prominent pattern in the velocity mismatch where BEDMAP2 ignores pinning points.

It is obvious from surface velocity observations that the eastern ice shelf of TWG moves at much lower rates than the western parts. Towards the ice margin, observed flow magnitudes decrease significantly and the flow directions are deviated zonally. Flow resistance, there, arises from an ice rise near the marine shelf front (Rignot, 2001; Rignot et al., 2014). Since this ice rise is absent in BEDMAP2, it gives an explanation for the high RMS deviation between observed and modelled surface velocities on this shelf (Table 1, Fig. 6). Nowhere else on Antarctica, we find as widespread and high differences largely exceeding 100 $\mathrm{m\,a^{-1}}$. Near the ice front, velocities are overestimated while upstream of this narrow zone, inferred velocities are too low. As observed and modelled velocities cannot be conciliated, we consider that this ice rise has an important influence on ice dynamics of the entire eastern ice shelf and the upstream grounded ice flow. For other less influential pinning points not included in BEDMAP2, we expect a much less pronounced mismatch pattern.

For the Bawden ice rise (BIR) on the northern part of the LC ice shelf, BEDMAP2 shows no contact between the ice and the bathymetry (Fig. 3). Similar to the TWG setup, this pinning point is located close to the marine ice front. As basal friction there is kept zero during our inversion, the model overestimated ice velocities in its vicinity by more than 100 $\mathrm{m\,a^{-1}}$. The spatial extent of this velocity mismatch reaches some 50 km upstream. Further upstream, no distinct pattern for underestimation emerges as was found for TWG. In this context, it is striking that the effect on the viscosity parameter $B$ reaches much further upstream. This might suggest that pinning points could be identified more directly from $B$. For the whole of Antarctica, we however find that elevated viscosity values, as found in this region on LC, are not necessarily associated to pinning points but rather point to meteoric origins and little shearing of this ice.

On the BSW ice shelf, ice flow is opposed by the McDonald Ice Rumples (MIR), near the southwestern marine front (Fig. 5). Again these are absent in BEDMAP2 and the velocity mismatch increases gradually, just exceeding 100 $\mathrm{m\,a^{-1}}$ near the ice front. At the same position we find a surface depression or a local thickness minimum. Yet, a similar geometry feature is not confirmed for BIR and for another prominent pinning point on Shakelton ice shelf. The latter even coincides with a local maximum in shelf thickness. Therefore, the velocity mismatch pattern is considered as characteristic for pinning points close to the marine shelf front that are unaccounted for in the inversion.

The majority of additional pinning points is clearly located near the shelf fronts (Fig. 1), but there are certainly many points away from both the marine fronts and the grounding line. For these points, we generally find that the remaining velocity mismatch compares to or falls below typical shelf RMS values (Figs. 3, 6, 7 and Table 1). Therefore, it is difficult to discern these features from the mismatch map. Neither are they strongly imprinted in the viscosity field. This either indicates that they are not as decisive for shelf dynamics or that our flow model can account for their effect in a different way. Further inland, shelf ice generally experiences more resistance, thus ice motion is slower and any model mismatch will be less expressed. Moreover, it is more likely that multiple sources provide resistance to a certain location on the shelf. Consequently, this superposition gives the inversion a possibility to conceal a missing pinning point by adjusting the weighting of various resistance sources via the viscosity parameter.

### 3.5 Introduction of missing pinning points

In this section, we want to shed light on how pinning points that are not in the geometry input can be included in the data assimilation. We have complementary information, around the whole of Antarctica, on where the shelves run aground (Sect. 2.4). Yet this information only holds their position but no details on the bathymetry. Therefore, the aim is to include these pinning points without changing the geometry input to the inversion.

As the BEDMAP2 geometry comes on 1 km grid-spacing, DInSAR-inferred grounded points Rignot et al. (2011a) laying within 1 km of the grounded area in BEDMAP2 are here considered as redundant information and excluded. In this way, we deliberately ignore any inland migration of the grounding line from the BEDMAP2 state. Almost half of the newly identified grounded shelf positions are located within 2 km of grounded parts of the ice sheet. As the BEDMAP2 geometry is primarily gridded on 5 km resolution and only in a final step rendered at 1 km for its final release, many of these identified points will be associated with grounding line migration or are a simple relict from inherent interpolations. Therefore, we use two other radii for excluding additional grounding line information, namely 5 and 10 km (Fig. 1). These three choices are referred to as PIN1, PIN5 and PIN10 and they hold respectively 121 838, 21 790 and 6 651 of the Rignot et al. (2011a) data points. The information, on where the ice shelves have bed contact, enters the inversion naturally by allowing a local optimisation of the basal friction coefficient $\beta^2$. As these pinning points cover only a few grid points, we ignore them in the regularisation term $J_{\beta^2}^{\mathrm{reg}}$ for basal friction.

Introducing ice rises in this way, the bulk velocity RMS deviation on the ice shelves is not necessarily improved (Table 1). It depends on the selected radius and only PIN5 shows a clear improvement. PIN5 also facilitates the inversion on a shelf-to-shelf basis. For any radius, the RMS deviation on the TWG ice shelf is reduced significantly, reaching a factor of $\sim 3$. From this fact, we conclude that the ice rise in this region has an important influence on the shelf dynamics of the eastern region and on the upstream grounded flow. We assume that introducing friction on many shelf locations just a few kilometres downstream of the BEDMAP2 grounding line is not conducive to the inversion, as many of these points are potential artefacts from data interpolation. PIN10 is largely free of such erratic friction points as most pinning points lie far out in the shelves.

We want to further justify our simple approach by showing the improvement for individual pinning points. On LC ice shelf, the mismatch upstream of BIR is virtually removed (Fig. 3e and f). In addition, the inferred viscosity parameter is regionally lowered and hence more consistent with the surroundings (Fig. 3b and c). On the Brunt ice shelf, a similar improvement in the velocity mismatch is seen upstream of the MIRs. The introduction of friction beneath the ice rise of TWG alters the flow field on the eastern part of the ice shelf significantly (Fig. 6a and b). As ice flow is inhibited, flow lines get more aligned with observations and turn away from the basal obstacle. The only distinct feature remaining in the velocity differences is an underestimation in the centre of the shelf, i.e. in the transition zone between the western unconfined shelf and these eastern parts. Similar patterns are seen along lateral shear margins downstream of other fast flowing outlet glaciers (Sect. 3.3). Despite the good performance of our approach in these regions, the inversion is hardly improved for many other regions where there is evidence for a pinning point (Fig. 7). One obvious reason for no improvement is that the mismatch was already small before accounting for these points. Moreover, these pinning features often have a small spatial extent, which is more or less well resolved dependent on where the model grid points fall. Another reasons is that the inversion might not be sufficiently converged such that these small-scale features would become relevant in the optimisation.

### 3.6 Identification of uncharted pinning points

The aim of this section is to use the velocity mismatch map to identify other potential pinning points. Here, we limit our analysis to pinning points close to the shelf fronts, where our approach tends to produce a characteristic signal in the difference map of modelled and observed velocities. There the signal is also expected to be most pronounced. In addition to the mismatch information, we verify that observed surface velocities actually decrease gradually towards the respective shelf front. The identification is performed manually because there are some features that clearly arise from the compilation of the velocity mosaic. A good example is BSW ice shelf (Fig. 5), where the mismatch map shows an erratic alternation near the northern shelf front that is traced back to different sensors and acquisition dates. A similar artificial pattern is found close to the front of Ross ice shelf, east of Roosevelt Island (Fig. 1).

We identify 7 locations around Antarctica (Table 2, Fig. 7), where there is strong evidence for resistance to the shelf flow and thus for a potential pinning point (PPP). Unfortunately, none of these features is directly crossed by Operation Ice Bridge flight lines. Neither are they found to be attributed to geographic names. The first feature, PPP1, is located at the eastern part of the marine front of Fimbul ice shelf (Queen Maud Land), north of Tsiolkovskiy and Kroshka islands (SCAR Gazetteer, US Board on Geographic Names). SCAR Gazetteer actually comprises an object at this location called Avrora Dome, giving first evidence for a topographic expression of this object. As a surface expression can be identified from satellite imagery, data from the RADARSAT-1 Antarctic Mapping Project (RAMP, Jezek and RAMP Product Team, 2002) and the Landsat Image Mosaic of Antarctica (LIMA, Bindschadler et al., 2008) is consulted (Fig. 8). On Fimbul ice shelf, the imagery highlights several surface features where we observe maximum velocity mismatch after the inversion. As these features are close to each other, we cannot discern if one of them is dominant for the upstream ice shelf flow. The two PPPs on Mushketov ice shelf are further apart ($\sim 5$ km) and are both well imprinted in the velocity mismatch map. On Venable ice sheet, the satellite image shows a very gradual imprint of PPP7, while on West ice shelf, the surface is highly crevassed near PPP4. These differences in the surface expression of pinning points pose a challenge if satellite imagery alone was used for their identification. In fact, the surface elevation product of BEDMAP2 already holds a rise of $\sim 3$ m above PPP1 (Table 2). Except for PPP5 on Shakelton ice shelf, we confirm similar topographic rises in BEDMAP2 at the locations of all the other features.

Complementary support for this interpretation, we find in a recent International Bathymetric Chart of the Southern Ocean (IBCSO: Arndt et al., 2013). It is a comprehensive compilation of bathymetric data around Antarctica. Its sub-shelf bathymetry is however inherited from BEDMAP2. On the ocean side of Fimbul ice shelf front, the map shows a bathemetric rise just offshore of PPP1 reaching up to $-190$ m below present sea level. The lower surface of the BEDMAP2 ice shelf reaches down to $-210$ m. Turning to PPP2 and PPP3, the BEDMAP2 ocean is very shallow ($< -100$ m). The IBCSO bathymetry is significantly deeper there, often by more than 200 m, showing two distinct rises reaching about $-190$ m in close vicinity of PPP3. Also at the other PPP locations, IBCSO indicates offshore rises in the bathymetry that match these locations and that are underestimated or ignored in BEDMAP2.

## 4 Summary and conclusions

We present a data assimilation approach for the Antarctic ice sheet, inferring two variables simultaneously, namely the basal friction coefficient and the ice viscosity parameter. After convergence, the underlying cost function is reduced by more than 3 orders of magnitude. For the whole of Antarctica, the RMS deviation in the velocity components attains ±12.3 $\mathrm{m\,a^{-1}}$, a factor 3 lower than for a recent comparable inversion (Arthern et al., 2015). The match is better on the grounded parts of the ice sheet, while it reaches an average of ±16.7 $\mathrm{m\,a^{-1}}$ for all ice shelves. In other studies, similar inversion were conducted to infer the viscosity field of individual shelves (Larour et al., 2005; Borstad et al., 2013; Larour et al., 2014). The general pattern of our inferred viscosity maps agrees well with these regional studies. Yet, our approach seems much more converged as the bulk RMS mismatch between modelled and observed velocities for these shelves is significantly lower. Often we state an improvement by more than a factor of 2. In addition, the inversion problem is sufficiently conditioned by a dual regularisation and a well-founded initial guess for the two variables. On the shelves, the final viscosity map is mostly unaffected by three variants for initialising the field.

As any model application on observed geometries requires an assumption on the ice density, we present several options to guarantee flotation of the shelf geometry in the model. Our results suggest that the thickness product from the BEDMAP2 data set is preferable for the performance of the inversion. If the BEDMAP2 geometry is directly taken and not adjusted for flotation, the inferred shelf viscosity is systematically biased. In our case, putting the shelves afloat involves a general lowering of the upper surface and, after inversion, much softer shelf ice as compared to the unadjusted case.

Remaining velocity differences exhibit uncommonly high magnitudes for the shelf of Thwaites Glacier (TWG), resulting in a bulk RMS mismatch of $\sim 80\,\mathrm{m\,a^{-1}}$, a maximum for the Antarctic shelves. The mismatch is actually limited to the eastern part of this shelf, where values typically exceed 100 $\mathrm{m\,a^{-1}}$. The differences there arise from an ice rise (Rignot et al., 2014), not included in BEDMAP2 and thus unaccounted for in our inversion. As the mismatch is particularly pronounced in this region, this ice rise certainly exerts strong control on the upstream shelf dynamics and, by extension on the flow of the grounded ice sheet. Therefore, an approach is forwarded that can account for pinning points not present in BEDMAP2 during the inversion, without adapting the geometry. Applying this approach, the bulk RMS for the TWG ice shelf is reduced to $\sim 30\,\mathrm{m\,a^{-1}}$. For other shelves, the improvement is not as expressed but still local mismatches are efficiently removed. Prominent examples are the Bawden ice rise on Larsen C and the McDonald ice rumples on Brunt ice shelf. For the whole of the Antarctic ice shelves, the RMS deviation is only moderately reduced to $16.4\,\mathrm{m\,a^{-1}}$.

We are also able to identify a characteristic pattern in the velocity mismatch where the BEDMAP2 geometry ignores the presence of pinning points close to the marine shelf front. This information is used in a final step to identify potential pinning points not included in the data sources at hand. We locate 7 features around Antarctica that provide prominent flow resistance. Though the identification could be done on the sole basis of the velocities observations or even directly from RADARSAT imagery, our approach implicitly quantifies the effect of these pinning points on ice dynamics. However, our identification does not claim to be complete. It should rather serve to highlight locations relevant for shelf dynamics. Our identification will miss out on ephemeral features that only appear in velocity observations if data acquisition falls into periods of actual ice/bed contact. In addition, our method is less efficient for pinning points away from the ice front because, there, ice flow is more likely experiencing multiple sources of resistance that reduces the signal amplitude.

The interpretation of the 7 features as pinning points is substantiated by the BEDMAP2 surface topography, that indicates topographic rises of several meters for 6 of them. Their surface expressions are also visible in RAMP and LIMA satellite imagery. For further evidence, these features could be delineated by means of differential InSAR data (e.g. Rignot et al., 2011a). If the bed contact was confirmed, only in-situ measurements could answer to what extent these pinning points pierce the ice body. Yet, such measurements are sparse in Antarctica, meaning that the bathymetry of the ocean cavities beneath the ice shelves is just not known in many places. The BEDMAP2 sub-shelf bathymetry is mostly inherited from the original BEDMAP data set (Lythe and Vaughan, 2001) and is based on an simple interpolation between the ice thickness at the grounding line and the seabed near the shelf front. This interpolation regularly spans 100 km. Actual measurements from seismic soundings were limited to Filchner-Ronne, Ross, Amery and the Larsen shelves. For the majority of the ice shelves, this original bathymetry was kept in BEDMAP2 though excavated by 20 m, in places where flotation was violated, as suggested by Le Brocq et al. (2010). In the meantime, Operation Ice Bridge collected free-air gravimetry data, primarily in West Antarctica, from which the bathymetry beneath entire shelves were inferred (Tinto and Bell, 2011; Cochran and Bell, 2012). Large areas could be covered with this airborne sensor. As the accuracy of this technique is not very high (Brisbourne et al., 2014), on-site seismic measurements should complement this data for the most prominent pinning points.

Finally, we want to acknowledge the many years and decades of data acquisition on Antarctica, which are a prerequisite to this study. Data compilation products for ice geometry and ice velocities are now available on comparable resolution (Morlighem et al., 2010; Rignot et al., 2011b; Fretwell et al., 2013), which triggered ice sheet-wide assimilations necessary to determine not well constrained parameters in ice flow models (e.g. Gillet-Chaulet et al., 2012; Morlighem et al., 2013; Arthern et al., 2015). The data assimilation, presented here, has reached a quality such that it can serve to identify inconsistencies in and between the velocity and geometry data sets. As the optimisation primarily addresses velocity differences, our assimilation reveals inhomogeneities in the surface velocity mosaic. But more importantly, it points towards regions where observed ice flow is not reconcilable with the geometric data base. This is especially the case for pinning points which can alter the dynamics of a larger area. Consequently, ice flow models require the location and extent of these pinning areas as input, in order to be able to reproduce observed velocities. Only then, realistic stress distributions could be inferred, which would make it possible to quantify the resistance that ice shelves exert on the upstream flow. For reliable model projections of pinned ice shelves and their upstream tributaries, the exact bathymetry of the bed contact is a prerequisite, as it determines the timing of a potential future ungrounding. This is examplified by the TWG setup. Despite our good knowledge on the spatial extent of this ice rise (Rignot, 2001; Rignot et al., 2014), we hardly have information on how much it actually protrudes the ice shelf. Any approach to model its future response is, at least, controversial. Once the shelves becomes ungrounded, we expect a significant acceleration reaching up to the grounded ice sheet and, consequently, a retreat of the grounding line (Favier et al., 2012). For TWG and actually for many glacier in the ASS, grounding line retreat leads into deeper bathymetry, which facilitates increasing ice export over the grounding line (e.g. Schoof, 2007). This provides a positive feedback on further acceleration and retreat, often associated with an inherent instability of the entire West Antarctic ice sheet (Bamber et al., 2009; Joughin et al., 2014). In this light, we want to put forward an appeal for a coordinated effort to produce a contemporaneous, high-resolution data set for ice geometry, ice dynamics and sub-shelf bathymetry in this region. In extension, additional observations on the exact geometry of pinning points not in BEDMAP2 is highly anticipated by the model community, because these features can affect the dynamics of entire ice shelves. Priority could be given to the pinning points that give rise to a large velocity mismatch if not accounted for in the presented data assimilation.

*Acknowledgements.* This study was funded by the French National Research Agency (ANR) under the SUMER (Blanc SIMI 6) 2012 project referenced as ANR-12-BS06-0018. Results presented in this publications are based on numerical simulation performed at the CIMENT (Calcul Intensif Modélisation Expérimentation Numérique et Technologique) high-performance computing centre of the Grenoble University, which is supported on local, county and regional level via the CIRA project (Calcul intensif en Rhône Alpes), and at the CINES (Centre Informatique National de l â Enseignement Supérieur) computing centre under allocation 2015-016066 from GENCI (Grand Equipement National de Calcul Intensif). Results presented here also received support and benefited from the development team at the CSC-IT Center for Science Ltd (Finland).

## References

Armstrong, T., Roberts, B., and Swithinbank, C.: Proposed new terms and definitions for snow and ice features, Polar Rec., 18, 501–502, 1977. 1463

Arndt, J., Schenke, H., Jakobsson, M., Nitsche, F., Buys, G., Goleby, B., Rebesco, M., Bohoyo, F., Hong, J., Black, J., Greku, R., Udintsev, G., Barrios, F., Reynoso-Peralta, W., Taisei, M., and Wigley, R.: The International Bathymetric Chart of the Southern Ocean (IBCSO) version 1.0: a new bathymetric compilation covering circum-Antarctic waters, Geophys. Res. Lett., 40, 3111–3117, doi:10.1002/grl.50413, 2013. 1482

Arthern, R. and Gudmundsson, G.: Initialization of ice-sheet forecasts viewed as an inverse Robin problem, J. Glaciol., 56, 527–533, doi:10.3189/002214310792447699, 2010. 1467

Arthern, R., Hindmarsh, R., and Wilams, R.: Inversion for the three dimensional velocity field of the Antarctic ice sheet, J. Geophys. Res., in preparation, 2015. 1464, 1467, 1472, 1474, 1483, 1485

Bamber, J., Riva, R., Vermeersen, B., and LeBrocq, A.: Reassessment of the potential sea-level rise from a collapse of the West Antarctic Ice Sheet, Science, 324, 901–903, doi:10.1126/science.1169335, 2009. 1486

Berthier, E., Scambos, T., and Shuman, C.: Mass loss of Larsen B tributary glaciers (Antarctic Peninsula) unabated since 2002, Geophys. Res. Lett., 39, L13501, doi:10.1029/2012GL051755, 2012. 1475

Bindschadler, R., Vornberger, P., Fleming, A., Fox, A., Mullins, J., Binnie, D., Paulsen, S., Granneman, B., and Gorodetzky, D.: The Landsat image mosaic of Antarctica, Remote Sens. Environ., 112, 4214–4226, doi:10.1016/j.rse.2008.07.006, 2008. 1482

Borstad, C. P., Rignot, E., Mouginot, J., and Schodlok, M. P.: Creep deformation and buttressing capacity of damaged ice shelves: theory and application to Larsen C ice shelf, The Cryosphere, 7, 1931–1947, doi:10.5194/tc-7-1931-2013, 2013. 1466, 1468, 1471, 1473, 1475, 1476, 1483

Brisbourne, A. M., Smith, A. M., King, E. C., Nicholls, K. W., Holland, P. R., and Makinson, K.: Seabed topography beneath Larsen C Ice Shelf from seismic soundings, The Cryosphere, 8, 1–13, doi:10.5194/tc-8-1-2014, 2014. 1485

Cochran, J. and Bell, R.: Inversion of IceBridge gravity data for continental shelf bathymetry beneath the Larsen Ice Shelf, Antarctica, J. Glaciol., 58, 540–552, doi:10.3189/2012JoG11J033, 2012. 1485

Craven, M., Allison, I., Fricker, H., and Warner, R.: Properties of a marine ice layer under the Amery Ice Shelf, East Antarctica, J. Glaciol., 55, 717–728, 2009. 1469

Depoorter, M., Bamber, J., Griggs, J., Lenaerts, J., Ligtenberg, S., van den Broeke, M., and Moholdt, G.: Calving fluxes and basal melt rates of Antarctic ice shelves, Nature, 502, 89–93, doi:10.1038/nature12567, 2013. 1463

Favier, L., Gagliardini, O., Durand, G., and Zwinger, T.: A three-dimensional full Stokes model of the grounding line dynamics: effect of a pinning point beneath the ice shelf, The Cryosphere, 6, 101–112, doi:10.5194/tc-6-101-2012, 2012. 1463, 1486

Fretwell, P., Pritchard, H. D., Vaughan, D. G., Bamber, J. L., Barrand, N. E., Bell, R., Bianchi, C., Bingham, R. G., Blankenship, D. D., Casassa, G., Catania, G., Callens, D., Conway, H., Cook, A. J., Corr, H. F. J., Damaske, D., Damm, V., Ferraccioli, F., Forsberg, R., Fujita, S., Gim, Y., Gogineni, P., Griggs, J. A., Hindmarsh, R. C. A., Holmlund, P., Holt, J. W., Jacobel, R. W., Jenkins, A., Jokat, W., Jordan, T., King, E. C., Kohler, J., Krabill, W., Riger-Kusk, M., Langley, K. A., Leitchenkov, G., Leuschen, C., Luyendyk, B. P., Matsuoka, K., Mouginot, J., Nitsche, F. O., Nogi, Y., Nost, O. A., Popov, S. V., Rignot, E., Rippin, D. M., Rivera, A., Roberts, J., Ross, N., Siegert, M. J., Smith, A. M., Steinhage, D., Studinger, M., Sun, B., Tinto, B. K., Welch, B. C., Wilson, D., Young, D. A., Xiangbin, C., and Zirizzotti, A.: Bedmap2: improved ice bed, surface and thickness datasets for Antarctica, The Cryosphere, 7, 375–393, doi:10.5194/tc-7-375-2013, 2013. 1463, 1464, 1468, 1485

Gagliardini, O. and Zwinger, T.: The ISMIP-HOM benchmark experiments performed using the Finite-Element code Elmer, The Cryosphere, 2, 67–76, doi:10.5194/tc-2-67-2008, 2008. 1465

Gagliardini, O., Zwinger, T., Gillet-Chaulet, F., Durand, G., Favier, L., de Fleurian, B., Greve, R., Malinen, M., Martín, C., Råback, P., Ruokolainen, J., Sacchettini, M., Schäfer, M., Seddik, H., and Thies, J.: Capabilities and performance of Elmer/Ice, a new-generation ice sheet model, Geosci. Model Dev., 6, 1299–1318, doi:10.5194/gmd-6-1299-2013, 2013. 1465, 1467

Gillet-Chaulet, F., Gagliardini, O., Seddik, H., Nodet, M., Durand, G., Ritz, C., Zwinger, T., Greve, R., and Vaughan, D. G.: Greenland ice sheet contribution to sea-level rise from a new-generation ice-sheet model, The Cryosphere, 6, 1561–1576, doi:10.5194/tc-6-1561-2012, 2012. 1465, 1466, 1467, 1485

Hansen, P.: Analysis of discrete ill-posed problems by means of the L-curve, SIAM Rev., 34, 561–580, doi:10.1137/1034115, 1992. 1472

Hindmarsh, R.: The role of membrane-like stresses in determining the stability and sensitivity of the Antarctic ice sheets: back pressure and grounding line motion, Philos. T. R. Soc. A, 364, 1733–1767, doi:10.1098/rsta.2006.1797, 2006. 1463, 1466

Holt, J., Blankenship, D., Morse, D., Young, D., Peters, M., Kempf, S., Richter, T., Vaughan, D., and Corr, H.: New boundary conditions for the West Antarctic Ice Sheet: subglacial topography of the Thwaites and Smith glacier catchments, Geophys. Res. Lett., 33, L09502, doi:10.1029/2005GL025561, 2006. 1469

Humbert, A., Kleiner, T., Mohrholz, C., Oelke, C., Greve, R., and Lange, M.: A comparative modeling study of the Brunt Ice Shelf/Stancomb-Wills Ice Tongue system, East Antarctica, J. Glaciol., 55, 53–65, doi:10.3189/002214309788608949, 2009. 1476

Jansen, D., Kulessa, B., Sammonds, P., Luckman, A., King, E., and Glasser, N.: Present stability of the Larsen C ice shelf, Antarctic Peninsula, J. Glaciol., 56, 593–600, doi:10.3189/002214310793146223, 2010. 1475

Jay-Allemand, M., Gillet-Chaulet, F., Gagliardini, O., and Nodet, M.: Investigating changes in basal conditions of Variegated Glacier prior to and during its 1982–1983 surge, The Cryosphere, 5, 659–672, doi:10.5194/tc-5-659-2011, 2011. 1472

Jezek, K. and RAMP Product Team: RAMP AMM-1 SAR Image Mosaic of Antarctica. Version 2, Alaska Satellite Facility, in association with the National Snow and Ice Data Center, Boulder, CO, USA, 2002. 1482

Joughin, I.: Ice-sheet velocity mapping: a combined interferometric and speckle-tracking approach, Ann. Glaciol., 34, 195–201, doi:10.3189/172756402781817978, 2002. 1475

Joughin, I., Smith, B., and Holland, D.: Sensitivity of 21st century sea level to ocean-induced thinning of Pine Island Glacier, Antarctica, Geophys. Res. Lett., 37, L20502, doi:10.1029/2010GL044819, 2010. 1477

Joughin, I., Smith, B., and Medley, B.: Marine ice sheet collapse potentially under way for the Thwaites Glacier Basin, West Antarctica, Science, 344, 735–738, doi:10.1126/science.1249055, 2014. 1486

Khazendar, A., Rignot, E., and Larour, E.: Larsen B Ice Shelf rheology preceding its disintegration inferred by a control method, Geophys. Res. Lett., 34, L19503, doi:10.1029/2007GL030980, 2007. 1475

Khazendar, A., Rignot, E., and Larour, E.: Roles of marine ice, rheology, and fracture in the flow and stability of the Brunt/Stancomb-Wills Ice Shelf, J. Geophys. Res., 114, F04007, doi:10.1029/2008JF001124, 2009. 1476

Kulessa, B., Jansen, D., Luckman, A., King, E., and Sammonds, P.: Marine ice regulates the future stability of a large Antarctic ice shelf, Nature Communications, 5, 3707, doi:10.1038/ncomms4707, 2014. 1475

Larour, E., Rignot, E., Joughin, I., and Aubry, D.: Rheology of the Ronne Ice Shelf, Antarctica, inferred from satellite radar interferometry data using an inverse control method, Geophys. Res. Lett., 32, L05503, doi:10.1029/2004GL021693, 2005. 1475, 1483

Larour, E., Khazendar, A., Borstad, C., Seroussi, H., Morlighem, M., and Rignot, E.: Representation of sharp rifts and faults mechanics in modeling ice shelf flow dynamics: application to Brunt/Stancomb-Wills Ice Shelf, Antarctica, J. Geophys. Res., 119, 1918–1935, doi:10.1002/2014JF003157, 2014. 1466, 1476, 1483

Le Brocq, A. M., Payne, A. J., and Vieli, A.: An improved Antarctic dataset for high resolution numerical ice sheet models (ALBMAP v1), Earth Syst. Sci. Data, 2, 247–260, doi:10.5194/essd-2-247-2010, 2010. 1485

Lythe, M. B. and Vaughan, D. G.: BEDMAP: a new ice thickness and subglacial topographic model of Antarctica, J. Geophys. Res., 106, 11335–11351, doi:10.1029/2000JB900449, 2001. 1485

MacAyeal, D.: Large-scale ice flow over a viscous basal sediment: theory and application to ice stream B, Antarctica, J. Geophys. Res., 94, 4071–4087, doi:10.1029/JB094iB04p04071, 1989. 1465

MacAyeal, D.: A tutorial on the use of control methods in ice sheet modelling, J. Glaciol., 39, 91–98, 1993. 1464, 1467

MacAyeal, D., Scambos, T. A., Hulbe, C. L., and Fahnestock, M. A.: Catastrophic ice-shelf break-up by an ice-shelf-fragment-capsize mechanism, J. Glaciol., 49, 22–36, doi:10.3189/172756503781830863, 2003 1475

Morlighem, M., Rignot, E., Seroussi, H., Larour, E., Ben Dhia, H., and Aubry, D.: Spatial patterns of basal drag inferred using control methods from a full-Stokes and simpler models for Pine Island Glacier, West Antarctica, Geophys. Res. Lett., 37, L14502, doi:10.1029/2010GL043853,, 2010. 1466, 1467, 1485

Morlighem, M., Seroussi, H., Larour, E., and Rignot, E.: Inversion of basal friction in Antarctica using exact and incomplete adjoints of a higher-order model, J. Geophys. Res., 118, 1746–1753, doi:10.1002/jgrf.20125, 2013. 1464, 1468, 1472, 1485

Paterson, W.: The Physics of Glaciers, Pergamon, Oxford, UK, 1994. 1466, 1468

Pritchard, H., Arthern, R., Vaughan, D., and Edwards, L.: Extensive dynamic thinning on the margins of the Greenland and Antarctic ice sheets, Nature, 461, 971–975, doi:10.1038/nature08471, 2009. 1469

Pritchard, H., Ligtenberg, S., Fricker, H., Vaughan, D., van den Broeke, M., and Padman, L.: Antarctic ice-sheet loss driven by basal melting of ice shelves, Nature, 484, 502–505, doi:10.1038/nature10968, 2012. 1469

Rignot, E.: Evidence for rapid retreat and mass loss of Thwaites Glacier, West Antarctica, J. Glaciol., 47, 213–222, doi:10.3189/172756501781832340, 2001. 1470, 1478, 1486

Rignot, E., Bamber, J., van den Broeke, M., Davis, C., Li, Y., van de Berg, W., and van Meijgaard, E.: Recent Antarctic ice mass loss from radar interferometry and regional climate modelling, Nat. Geosci., 1, 106–110, doi:10.1038/ngeo102, 2008. 1463

Rignot, E., Mouginot, J., and Scheuchl, B.: Antarctic grounding line mapping from differential satellite radar interferometry, Geophys. Res. Lett., 38, L10504, doi:10.1029/2011GL047109, 2011a. 1470, 1471, 1479, 1480, 1484, 1502

Rignot, E., Mouginot, J., and Scheuchl, B.: Ice flow of the Antarctic Ice Sheet, Science, 333, 1427–1430, doi:10.1126/science.1208336, 2011b. 1464, 1470, 1475, 1485

Rignot, E., Mouginot, J., Morlighem, M., Seroussi, H., and Scheuchl, B.: Widespread, rapid grounding line retreat of Pine Island, Thwaites, Smith, and Kohler glaciers, West Antarctica, from 1992 to 2011, Geophys. Res. Lett., 41, 3502–3509, doi:10.1002/2014GL060140, 2014. 1470, 1471, 1478, 1483, 1486

Rott, H., Skvarca, P., and Nagler, T.: Rapid collapse of northern Larsen Ice Shelf, Antarctica, Science, 271, 788–792, doi:10.1126/science.271.5250.788, 1996.

Rott, H., Müller, F., Nagler, T., and Floricioiu, D.: The imbalance of glaciers after disintegration of Larsen-B ice shelf, Antarctic Peninsula, The Cryosphere, 5, 125–134, doi:10.5194/tc-5-125-2011, 2011. 1475

Scambos, T., Bohlander, J., Shuman, C., and Skvarca, P.: Glacier acceleration and thinning after ice shelf collapse in the Larsen B embayment, Antarctica, Geophys. Res. Lett., 31, L18402, doi:10.1029/2004GL020670, 2004. 1475

Schoof, C.: Ice sheet grounding line dynamics: steady states, stability, and hysteresis, J. Geophys. Res., 112, F03S28, doi:10.1029/2006JF000664, 2007. 1463, 1486

Shepherd, A., Ivins, E., Geruo, A., Barletta, V., Bentley, M., Bettadpur, S., Briggs, K., Bromwich, D., Forsberg, R., Galin, N., Horwath, M., Jacobs, S., Joughin, I., King, M., Lenaerts, J., Li, J., Ligtenberg, S., Luckman, A., Luthcke, S., McMillan, M., Meister, R., Milne, G., Mouginot, J., Muir, A., Nicolas, J., Paden, J., Payne, A., Pritchard, H., Rignot, E., Rott, H., Sørensen, L., Scambos, T., Scheuchl, B., Schrama, E., Smith, B., Sundal, A., van Angelen, J., van de Berg, W., van den Broeke, M., Vaughan, D., Velicogna, I., Wahr, J., Whitehouse, P., Wingham, D., Yi, D., Young, D., and Zwally, H.: A reconciled estimate of ice-sheet mass balance, Science, 338, 1183–1189, doi:10.1126/science.1228102, 2012. 1463

Thomas, R.: Ice shelves: a review, J. Glaciol., 24, 273–286, 1979. 1463

Tinto, K. and Bell, R.: Progressive unpinning of Thwaites Glacier from newly identified offshore ridge: constraints from aerogravity, Geophys. Res. Lett., 38, L20503, doi:10.1029/2011GL049026, 2011. 1485

Van Der Veen, C.: Fundamentals of Glacier Dynamics, Taylor & Francis, Rotterdam, the Netherlands, 1999. 1466

Van Liefferinge, B. and Pattyn, F.: Using ice-flow models to evaluate potential sites of million year-old ice in Antarctica, Clim. Past, 9, 2335–2345, doi:10.5194/cp-9-2335-2013, 2013. 1468

Vaughan, D., Corr, H., Ferraccioli, F., Frearson, N., O'Hare, A., Mach, D., Holt, J., Blankenship, D., Morse, D., and Young, D.: New boundary conditions for the West Antarctic ice sheet: subglacial topography beneath Pine Island Glacier, Geophys. Res. Lett., 33, L09501, doi:10.1029/2005GL025588, 2006. 1469

Vieli, A., Payne, A., Du, Z., and Shepherd, A.: Numerical modelling and data assimilation of the Larsen B ice shelf, Antarctic Peninsula, Philos. T. R. Soc. A, 364, 1815–1839, doi:10.1098/rsta.2006.1800, 2006. 1475

Vieli, A., Payne, A., Shepherd, A., and Du, Z.: Causes of pre-collapse changes of the Larsen B ice shelf: numerical modelling and assimilation of satellite observations, Earth Planet. Sc. Lett., 259, 297–306, doi:10.1016/j.epsl.2007.04.050, 2007. 1475

**Table 1.** RMS deviation between simulated and observed velocity components for different regions. For the inversion, different option to ensure flotation on the ice shelves are assessed. As a reference, the input geometry is kept while assuming a constant ice density (BEDMAP2). A second option is to locally adjust the density field on the ice shelves according to flotation ($\mathbb{D}$). Otherwise, an a-priori adjustment of the geometry is necessary, keeping either the upper surface ($\mathbb{U}$), the lower surface ($\mathbb{L}$) or the thickness of the ice shelves ($\mathbb{T}$) from BEDMAP2. For initialising the viscosity parameter on the shelves, three options are assessed, based either on inferred ice temperatures (TB), on a local hydrostatic balance (HB) or on a compromise of both used to identify damaged ice (DC). Avoiding redundancy, complementary information on pinning points is excluded on the basis of how far they are away from grounded ice in BEDMAP2. Here we present results for 3 radii, 1, 5 and 10 km, respectively referred to as PIN1, PIN5 PIN10.

| ice geometry | BEDMAP2 | $\mathbb{D}$-shelf | $\mathbb{U}$-shelf | $\mathbb{L}$-shelf | $\mathbb{T}$-shelf | $\mathbb{T}$-shelf | $\mathbb{T}$-shelf | PIN1 | PIN5 | PIN10 |
|---|---|---|---|---|---|---|---|---|---|---|
| initial viscosity | TB | TB | TB | TB | TB | DC | HB | TB | TB | TB |
| Region | | | | | | | | | | |
| Ross ice shelf | 12.2 | 13.2 | 12.3 | 17.7 | 11.5 | 11.5 | 11.5 | 11.7 | 11.5 | 11.8 |
| Filchner-Ronne ice shelf | 15.2 | 16.1 | 15.0 | 22.3 | 15.2 | 15.2 | 15.2 | 15.5 | 15.2 | 15.6 |
| Brunt/Stancomb-Wills ice shelf | 20.9 | 22.5 | 18.9 | 23.8 | 18.0 | 18.0 | 18.0 | 18.2 | 17.9 | 18.2 |
| Shakelton ice shelf | 33.4 | 33.9 | 31.4 | 36.6 | 29.6 | 29.6 | 29.6 | 29.9 | 29.6 | 30.0 |
| Amery ice shelf | 10.8 | 11.8 | 10.9 | 34.5 | 11.5 | 11.5 | 11.6 | 11.7 | 11.5 | 11.9 |
| Larsen C | 13.5 | 14.3 | 13.3 | 17.1 | 13.0 | 12.9 | 13.0 | 12.7 | 12.5 | 12.8 |
| Dotson ice shelf | 33.7 | 35.1 | 33.7 | 33.9 | 32.2 | 32.0 | 32.2 | 32.7 | 32.1 | 32.9 |
| Crosson ice shelf | 21.3 | 22.4 | 21.6 | 35.0 | 21.6 | 21.5 | 21.6 | 21.7 | 21.5 | 22.1 |
| Thwaites Glacier shelf | 78.4 | 88.1 | 85.9 | 104.8 | 78.5 | 79.6 | 80.0 | 32.2 | 31.8 | 32.4 |
| Pine Island Glacier shelf | 43.3 | 43.7 | 42.8 | 80.5 | 41.0 | 40.8 | 40.9 | 41.5 | 41.2 | 41.7 |
| Grounded part | 11.7 | 11.8 | 11.7 | 29.3 | 11.7 | 11.7 | 11.7 | 11.7 | 11.7 | 11.7 |
| Floating part | 17.1 | 19.6 | 17.1 | 28.1 | 16.7 | 16.7 | 16.7 | 16.7 | 16.4 | 16.8 |
| Antarctica | 12.4 | 13.0 | 12.5 | 29.2 | 12.4 | 12.4 | 12.4 | 12.4 | 12.3 | 12.4 |

**Table 2.** Decimal longitudinal and latitudinal range where we find evidence for potential pinning points (PPP). Also given are the respective shelf names. The ice shelf east of Verbyud island has no name. As its main tributary is Mushketov glacier, we refer to it as Mushketov ice shelf. If a peak in the BEDMAP2 surface elevation is found, its height is manually estimated with respect to the surrounding shelf surface. If no peak is identifiable, no number is given ("–").

| | Northern boundary | Southern boundary | Western boundary | Eastern boundary | Respective ice shelf | Height of topographic rise in BEDMAP2 |
|---|---|---|---|---|---|---|
| PPP1 | −70.12 | −70.19 | 2.26 | 2.50 | Fimbul ice shelf | ∼ 3 m |
| PPP2 | −69.73 | −69.77 | 17.27 | 17.42 | Mushketov ice shelf | ∼ 4 m |
| PPP3 | −69.70 | −69.74 | 17.52 | 17.71 | Mushketov ice shelf | ∼ 4 m |
| PPP4 | −67.35 | −67.54 | 81.39 | 81.80 | West ice shelf | ∼ 15 m |
| PPP5 | −66.20 | −66.27 | 95.36 | 95.60 | Shakelton ice shelf | – |
| PPP6 | −75.36 | −75.47 | −145.20 | −144.73 | Nickerson ice shelf | ∼ 5 m |
| PPP7 | −72.92 | −72.97 | −86.66 | −86.43 | Venable ice shelf | ∼ 10 m |

Title Page
Abstract
Introduction
Conclusions
References
Tables
Figures
◀▎
▶▎
◀
▶
Back
Close
Full Screen / Esc
Printer-friendly Version
Interactive Discussion

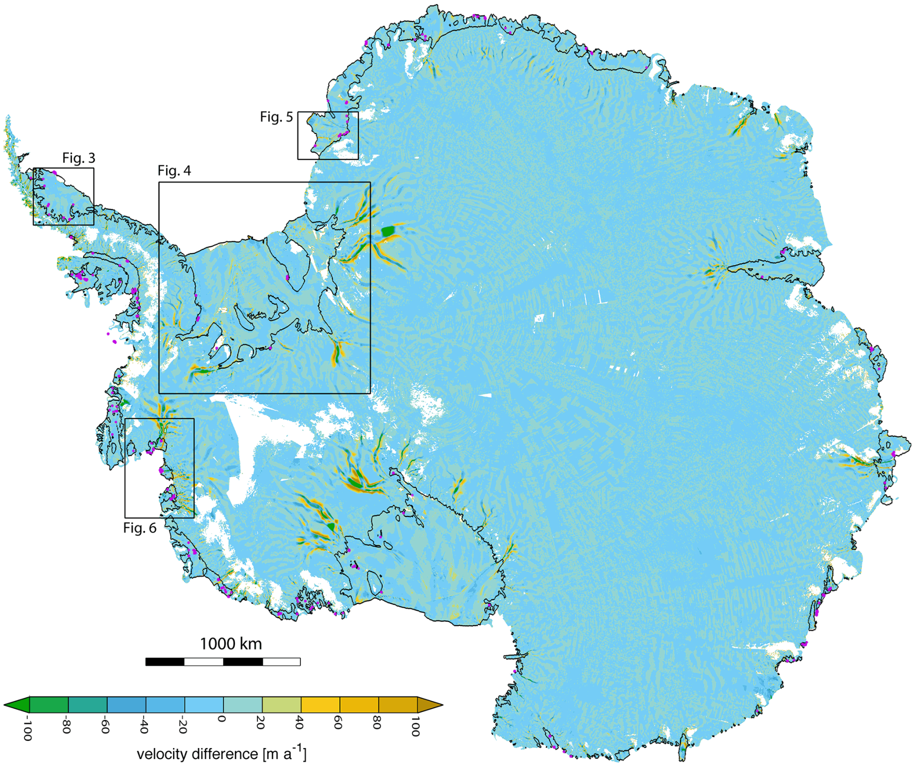

**Figure 1.** Difference between simulated and observed ice velocity magnitudes over the Antarctic ice sheet. The result is based on the $\mathbb{T}$-geometry accounting for complementary information on pinning points. White areas over ice-covered areas indicate regions without velocity information. Pink squares indicate observed grounding line locations not included in BEDMAP2 and further away than 5 km from grounded areas in BEDMAP2 (PIN5). The black contour line delineates the floating shelves. Black rectangles indicate locations of insets.

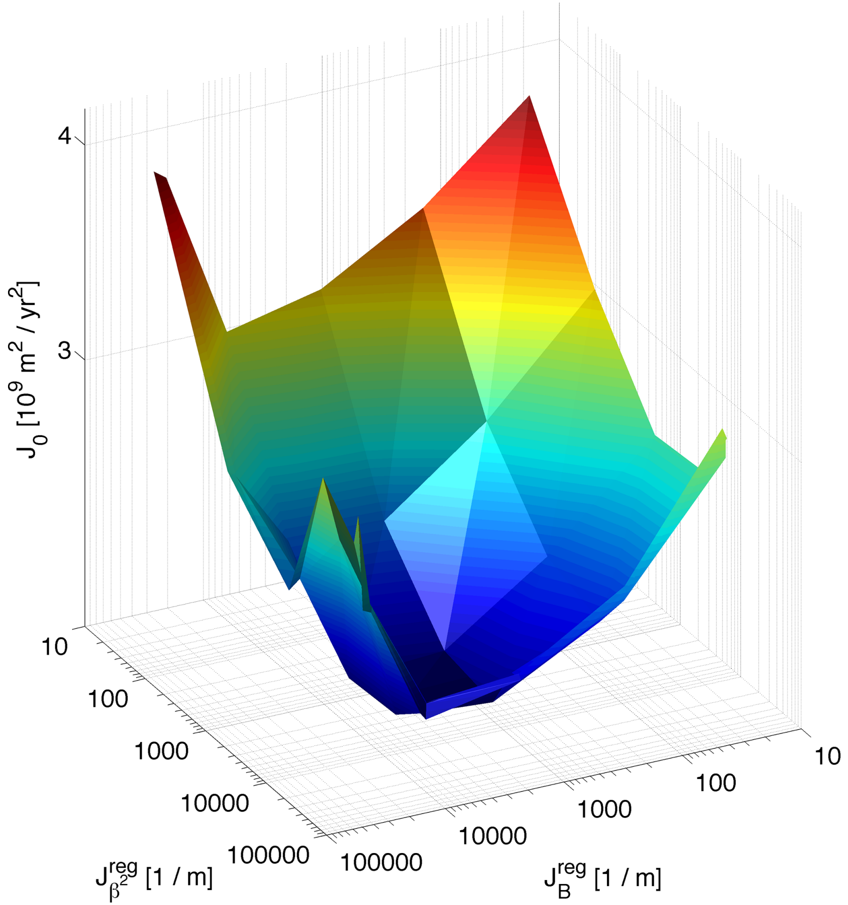

**Figure 2.** L-surface obtained for the simultaneous optimisation of two variables as a function of the respective regularisation terms.

Title Page
Abstract
Introduction
Conclusions
References
Tables
Figures
◀◀
▶▶
◀
▶
Back
Close
Full Screen / Esc
Printer-friendly Version
Interactive Discussion

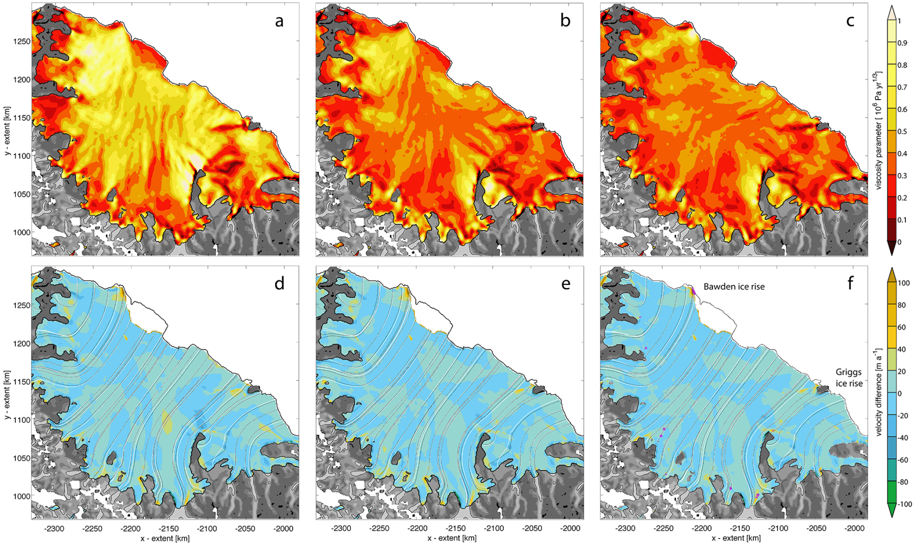

**Figure 3.** Ice viscosity parameter **(a–c)** as inferred by the control method for the Larsen C ice shelf. Velocity difference **(d–f)** as in Fig. 1. **(a, d)** show results based on the actual BEDMAP2 geometry, while **(b, e)** show results after flotation is guaranteed using the $\mathbb{T}$-method. Inversion results on Larsen C for the $\mathbb{T}$-geometry accounting for friction beneath pinning points not included in BEDMAP2 **(c, f)**. Gray shading indicates observed velocity magnitude on grounded parts of the ice sheet. The BEDMAP2 shelf extents is indicate by a black contour line. On the shelf, black dashed and white lines indicate respectively observed and modelled streamlines. The black dashed line on the grounded areas gives the 100 m a$^{-1}$ isoline of the observed surface velocities. Locations of pinning points (PIN5) not in BEDMAP2 are indicated with pink squares in **(e)**.

Title Page
Abstract Introduction
Conclusions References
Tables Figures
I◀ ▶I
◀ ▶
Back Close
Full Screen / Esc
Printer-friendly Version
Interactive Discussion

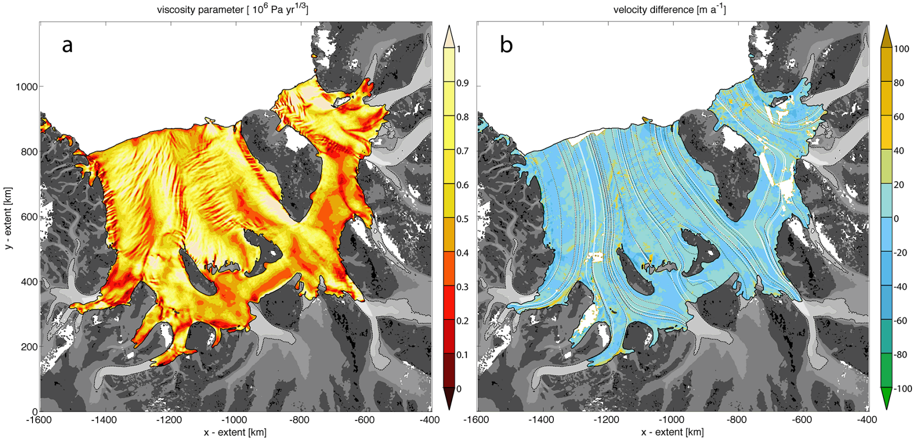

**Figure 4.** Ice viscosity parameter **(a)** and difference between simulated and observed ice velocity magnitudes **(b)** on Filchner-Ronne ice shelf. Shading and contour lines as in Fig. 3. Results are based on the $\mathbb{T}$-geometry without additional pinning points. White areas indicate regions without velocity information.

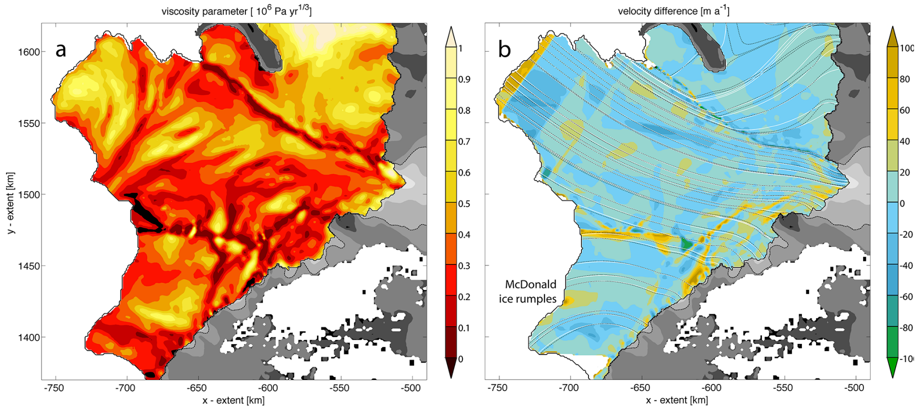

**Figure 5.** Ice viscosity parameter **(a)** and velocity differences **(b)** as in Fig. 4 for the Brunt/Stancomb-Wills ice shelf.

Title Page
Abstract
Introduction
Conclusions
References
Tables
Figures
|◀
▶|
◀
▶
Back
Close
Full Screen / Esc
Printer-friendly Version
Interactive Discussion

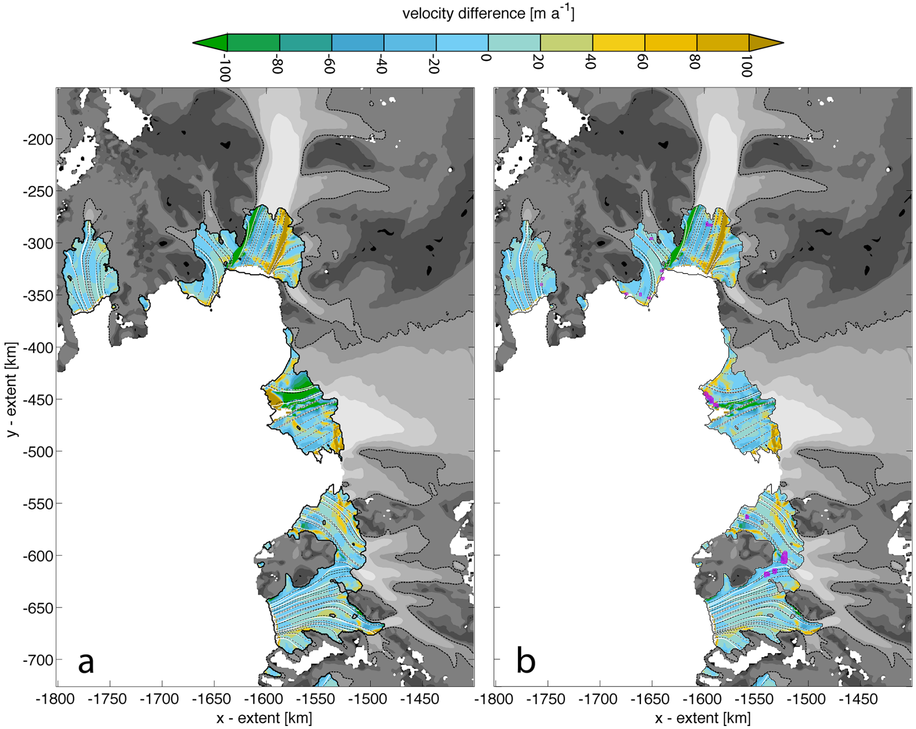

**Figure 6.** Velocity differences as in Fig. 4 for the ice shelves in the Amundsen Sea Embayment. Results are based on the 𝕋-geometry for the cases that additional pinning points (pink rectangles, PIN5) are not accounted for **(a)** or accounted for **(b)** in the inversion. Shading, contour lines and markers as in Fig. 3.

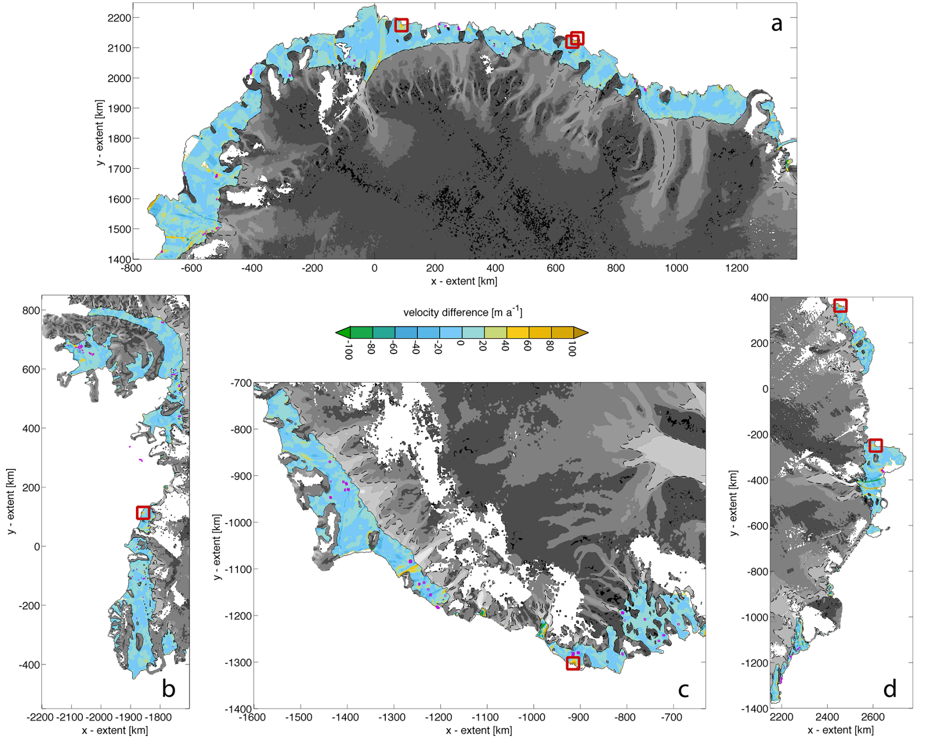

**Figure 7.** Velocity differences as in Fig. 4 for ice shelves in different regions around Antarctica: Queen Maud Land **(a)**, Palmer and Ellsworth Land **(b)**, Marie Byrd Land **(c)**, Wilhem II, Queen Mary and Wilkens Land **(d)**. Results are based on the $\mathbb{T}$-geometry when accounting for additional pinning points (PIN5) in the inversion. Shading, contour lines and markers as in Fig. 3. Dark red squares give the positions of the 7 potential pinning points identified in this study (Table 2).

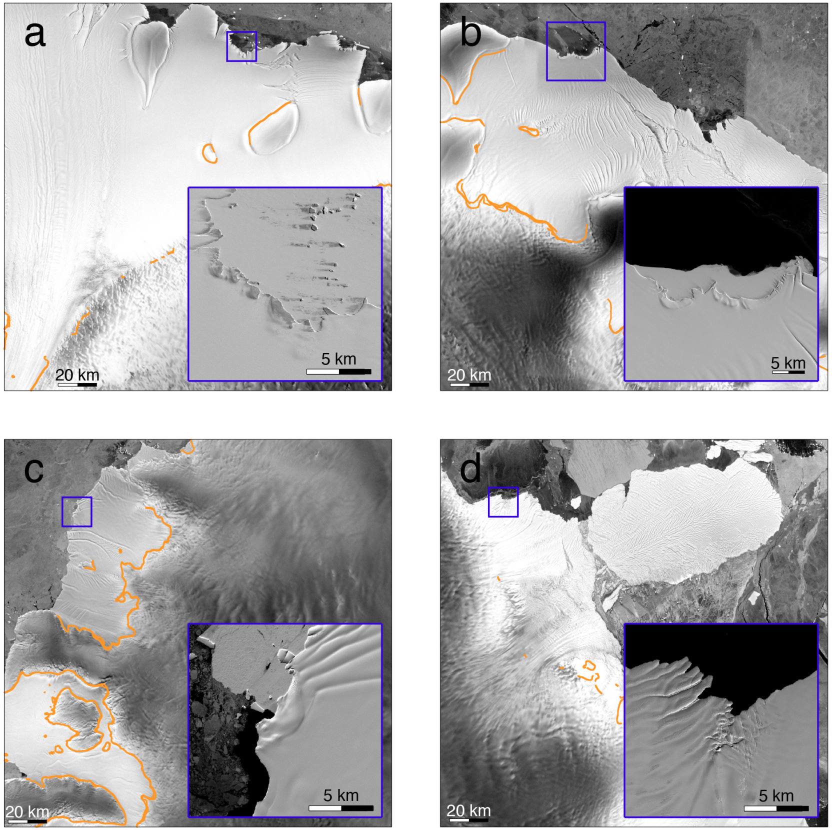

**Figure 8.** RAMP imagery for Fimbul **(a)**, Mushketov **(b)**, Venable **(c)** and West ice shelf **(d)**. Blue rectangles encircle the locations of the identified PPPs (Table 2). Insets show closeups of these locations with satellite imagery from LIMA. Orange lines delineate multi-year grounding line positions by Rignot et al. (2011a).